Strong-field photoemission from surfaces: Theoretical approaches

Sergey V. Yalunin,[1,2,*] Max Gulde,[2] and Claus Ropers[2,†]
[1]*Department of Physics, I. Kant Baltic Federal University, 236041 Kaliningrad, Russia*
[2]*Courant Research Center Nano-Spectroscopy and X-Ray Imaging, University of Göttingen, 37077 Göttingen, Germany*
(Received 24 May 2011; revised manuscript received 14 September 2011; published 7 November 2011)

The problem of highly nonlinear photoemission from a metal surface is considered using analytical and numerical approaches. Descriptions are found which cover both the weak-field and the strong-field regimes and the transition between them. The results of a time-dependent perturbation theory are in very good agreement with those from more numerically involved schemes, including a variational version of the Floquet method and a Crank-Nicolson-like numerical scheme. The implemented Crank-Nicolson variant uses transparent boundary conditions and an incident plane-wave state in the metal. Both numerical approaches give very similar results for weak and intermediate fields, while in the strong-field regime the Crank-Nicolson scheme is more effective than the Floquet method. We find an enhancement in the effective nonlinearity in the weak-field regime, which is caused by surface scattering of the final state. The presented theory also covers angular emission probabilities as a function of light intensity and explains an increase toward forward emission with growing field strength.

DOI: 10.1103/PhysRevB.84.195426 PACS number(s): 79.60.Jv, 42.65.Re, 73.20.Mf

I. INTRODUCTION

The study of atoms exposed to optical fields that greatly exceed the electronic binding fields has become increasingly important in the past two decades. With the availability of intense, ultrashort laser pulses, this has resulted in a rapid progress of strong-field atomic physics and led to a multitude of technological advances, for example, in the area of attosecond physics.[1] High-harmonic generation and photoelectron emission are two of the principal phenomena carrying signatures of strong-field interactions of light with bound electrons. While these effects are mostly studied in the gas phase, the interest in extending strong-field physics to surfaces and nanostructures is continually growing.

In terms of high harmonic generation, the solid state offers various promising alternatives, either in the form of plasma generation at surfaces[2] or, more recently, by using optical-field enhancements in nanostructures.[3] In the case of photoelectron emission from surfaces, some works study effects beyond threshold multiphoton photoemission,[4–10] although both optical damage and space-charge effects complicate observations. Single metallic nanotips have proven useful to study localized, nonlinear photoemission in a very controlled manner,[11–15] in part because they offer the possibility to tailor, enhance, and confine optical fields. The process of localized nonlinear photoelectron emission at nanostructures is attracting considerable interest, due to its relevance for high-brilliance, pulsed electron sources. Recent studies have illustrated the possibility to observe above-threshold and strong-field photoemission at such tips.[15,16] Despite this experimental progress in strong-field photoemission from nanostructures and surfaces, a unified description of the underlying mechanisms and the transition from the perturbative to the strong-field regimes is still missing. Because of the predominance of gas phase studies, the majority of theoretical works treat strong-field ionization from electrons bound to single-atom potentials.

Early theoretical works are mostly concerned with the conventional (i.e., linear) photoemission process.[17–19] One of the first physically motivated multiphoton considerations is found in Ref. 20, where a generalization of the Fowler-DuBridge theory[21] is presented. This generalization assumes that the photoemission is a linear combination of partial currents, each following a power-law dependence on the incident light intensity,[22] a result known from perturbation theory. A first nonperturbative treatment is carried out by Keldysh[23] in the context of atomic ionization, further developed in Refs. 24 and 25 and extended to the case of metals in Ref. 26. In principle, the Keldysh approach applies to cases where the photon energy is much lower than the electron binding energy and, therefore, requires the minimum number of absorbed photons to be large. Yet, the approach often produces accurate results also for relatively small absorbed photon numbers.[27] The large photon number condition was overcome by Reiss in Ref. 28, where generalized Bessel functions initially proposed in Ref. 29 are applied in the context of electron-positron pair creation. Recently, other approaches based on a Floquet analysis[30–32] and a direct numerical integration of the Schrödinger equation were presented.[33–37]

Here, we present a comprehensive theoretical treatment of weak-field (perturbative) and strong-field (tunneling) photoemission from surfaces and the transition between the two regimes, including several key aspects that differ from their gas phase counterparts. This includes surface effects, such as electron reflection and backscattering, as well as the use of delocalized initial states. Several theoretical methods which require varying degrees of analytical and numerical effort are examined, and their results are compared.

In the physical model considered, electrons are treated as free independent particles in the conduction band, and electron excitation takes place in the vicinity of the metal surface.[38–40] The induced time-dependent electric potential is taken in the dipole approximation and in the length gauge. The length gauge is known to be well suited for the description of above-threshold ionization in a perturbation-theory framework. In particular, for a short-range potential this was previously justified by comparisons with a numerical solution of the time-dependent Schrödinger equation[48] and with experimental findings.[49] We will see in Sec. IV that in the strong-field limit the length-gauge calculation reproduces the known static-field tunneling result. The manuscript is structured as follows.

Section II presents a time-dependent perturbation theory considering dipole transitions between initial plane-wave states in the solid and linear combinations of final Volkov states.[41] Here, we employ a modified strong-field approximation which takes into account electron reflection from the surface via a Green's function, which is constructed following an approach from Ref. 42. The Green's function describes the propagation of an electron in a time-periodic optical field. It is represented as an infinite sum over equally spaced energies (sidebands separated by the photon energy) and allows for a natural interpretation in terms of multiphoton absorption of different orders.

The total photoemission current and the angular distribution of the emitted electrons for a three-dimensional planar metal surface are analyzed in Sec. III. Section IV contains a derivation of the strong-field limit for oscillatory fields. In Sec. V, a variational approach based on the Floquet method is discussed, which matches wave functions at the interface between the solid and the vacuum.

An explicit integration of the Schrödinger equation in the Crank-Nicolson scheme is covered in Sec. VI for pulsed excitation. The special feature here is the use of transparent boundary conditions[44,45] that permit us to treat photoemission from delocalized initial conduction band states.

In Sec. VII, the numerical results and analysis of the developed approximations are presented and discussed. Section VIII concludes the paper. The three appendices provide details of the formulations: Appendix A gives insight into the Green's function calculation; Appendix B covers the details of the integration of a rapidly oscillating function; Appendix C provides the formulas of the variational approach in a form suitable for numerical evaluation. Atomic units are used throughout the paper unless indicated otherwise.

II. TIME-DEPENDENT PERTURBATION THEORY

First, consider photoelectron emission from metals by a light field with a single carrier frequency, characterized by the electric field $F(t) = F\cos\omega t$. The electric field is taken to be perpendicular to the metal surface and parallel to the z axis, aiming toward the vacuum region. We assume that electrons in the metal move freely, with an effective mass being identical to the rest mass in vacuum. The metal is characterized by the surface potential $U = -(E_F + W)$ with the Fermi energy E_F and the work function W. The surface interaction between the electron and the metal as well as the interaction with the electric field outside the metal, in the length gauge, are given by

$$V = -\begin{cases} zeF(t), & z \geqslant 0 \\ E_F + W, & z < 0, \end{cases} \tag{1}$$

where $e = -1$ for the electron. Presently, we do not consider the field penetration into the metal and the image potential,[46] so we neglect the Schottky effect (barrier reduction). The dipole approximation is justified because the distances essential for the photoemission process[47] are much smaller than typical optical wavelengths.

We begin our consideration of the photoemission process within a one-dimensional model. The relation to a three-dimensional treatment including experimentally observable quantities is discussed in Sec. III. The initial unperturbed state in the absence of the driving field is described by the wave function

$$\psi_0(z,t) = \exp(-iEt)\begin{cases} \exp(ikz) + R_0\exp(-ikz), & z < 0 \\ \frac{2ik}{ik-\alpha}\exp(-\alpha z), & z \geqslant 0, \end{cases} \tag{2}$$

where k denotes the initial momentum of the electron, $E = (1/2)k^2 + U$ is the energy of the initial state, $\alpha = \sqrt{-2E}$ denotes the decay length of the state in the vacuum region, and R_0 is the reflection amplitude. To calculate the emission probability in the presence of the time-periodic external field $F(t)$ one must solve the time-dependent Schrödinger equation

$$i\frac{\partial\psi}{\partial t} = \left(-\frac{1}{2}\frac{\partial^2}{\partial z^2} + V\right)\psi. \tag{3}$$

The eigenstates of Eq. (3) at positive z are known as Volkov states.[41] The Volkov state for a time-periodic potential is characterized by a quasienergy (Floquet eigenenergy), which is the sum of a drift kinetic energy and ponderomotive energy shift (electron quiver energy). The latter has a simple physical interpretation: when an electron is ejected in the presence of an intense optical field, the field accelerates the electron. If the interaction occurs continuously over several optical cycles, the electron undergoes oscillations. The ponderomotive energy shift is defined as the averaged energy over the electron oscillations.

In the length gauge, the Volkov states ψ_p^{V} with drift momentum p are given by

$$\psi_p^{\mathrm{V}} = \exp\left\{i[p + p_{\mathrm{cl}}(t)]z - \frac{i}{2}\int_0^t [p + p_{\mathrm{cl}}(\tau)]^2 d\tau\right\}. \tag{4}$$

The classical momentum p_{cl} of the electron oscillation in the electric field is given by

$$p_{\mathrm{cl}}(t) = \frac{eF}{\omega}\sin\omega t. \tag{5}$$

The lower limit of the integral in Eq. (4) introduces a constant phase factor and can therefore be chosen arbitrarily.

A. Analytical expression for time-periodic Green's function

In order to solve Eq. (3), we employ the Green's function approach. First, we introduce the time-periodic Green's function as a solution of the equation

$$\left(i\frac{\partial}{\partial t} + \frac{1}{2}\frac{\partial^2}{\partial z^2} - V\right)G(z,t;z',t') = \delta(z-z')\delta_p(t-t'), \tag{6}$$

where $\delta_p(t)$ denotes the periodic array of delta functions with the singularities at $t_m = mT$, $m \in \mathbb{Z}$, and T is the period of the field oscillations. Note that the required time-periodic, outgoing Green's function can be obtained within the strong-field approximation (SFA)[23–25,28] as described in Ref. 42. Finally, the Green's function can be represented as the infinite sum over sidebands (see Appendix A):

$$G^{\mathrm{SFA}}(z,t;z',t') = \sum_{n\in\mathbb{Z}}\frac{1}{ip_nT}\exp[i\Omega_n(t,t')] \times \exp[ip_n|s(z,t) - s(z',t')|], \tag{7}$$

in terms of the classical trajectory

$$s(z,t) = z - z_{\rm cl}(t), \quad z_{\rm cl}(t) = \int_0^t p_{\rm cl}(\tau)d\tau \tag{8}$$

of the electron in the electric field $F(t)$ and the time-dependent phase:

$$\Omega_n(t,t') = zp_{\rm cl}(t) - z'p_{\rm cl}(t') - \frac{1}{2}\int_{t'}^{t}\left[p_n^2 + p_{\rm cl}^2(\tau)\right]d\tau. \tag{9}$$

Note that a similar phase expression was also considered in Ref. 43, Eq. (2.10), in the context of a zero-range potential. To take into account photoemission as well as below-threshold excitation of electrons and emission of photons, we sum over positive and negative integers n. The drift momentum p_n (Re $p_n \geqslant 0$) is determined by the quasienergy condition

$$\tfrac{1}{2}p_n^2 + U_p = E + n\omega, \tag{10}$$

where U_p denotes the ponderomotive energy:

$$U_p = \frac{1}{2}\langle p_{\rm cl}^2\rangle = \frac{e^2F^2}{4\omega^2}. \tag{11}$$

Two comments regarding the strong-field approximation can be made now: first, $G^{\rm SFA}$ in Eq. (7) is an exact solution of Eq. (6) at positive z. Secondly, although this Green's function satisfies the outgoing-wave boundary condition at minus infinity, the approximation neglects the influence of the potential well, which is especially important in the weak-field regime.

In order to develop a more general quantitative theory embracing both tunneling and perturbative regimes, we propose the following analytic approximation for the time-periodic Green's function:

$$G(z,t;z',t') = \sum_{n\in\mathbb{Z}}\frac{1}{ip_nT}\exp[i\Omega_n(t,t')] \times \exp(ip_ns_>)\psi_{p_n}^{(-)}(s_<), \tag{12}$$

where $s_>$ and $s_<$ denote maximum and minimum values of $s(z,t)$ and $s(z',t')$, respectively. The function $\psi_{p_n}^{(-)}(s)$ is a linear combination of plane waves (the minus superscript indicates that this function controls the left boundary condition) given by

$$\psi_{p_n}^{(-)}(s) = \exp(-ip_ns) + R_n^{(1)}R_n^{(2)}\exp(ip_ns), \tag{13}$$

with

$$R_n^{(1)} = -\frac{k_n - p_n}{k_n + p_n}, \quad R_n^{(2)} = J_0\left(\frac{2p_neF}{\omega^2}\right), \tag{14}$$

and the momentum

$$k_n = \sqrt{p_n^2 + 2(U_p - U)}, \tag{15}$$

where $U = -(E_F + W)$ denotes the potential step at the surface. $J_0(x)$ is a Bessel function of zeroth order. Figure 1 shows a schematic of the Green's function containing outgoing and surface-reflected waves from a perturbation at s'. The most notable aspect of this Green's function is the reflection coefficient $R_n^{(1)}R_n^{(2)}$, which contains two components: $R_n^{(1)}$ plays the role of an elastic reflection amplitude in analogy with the one for a step-down potential, with momenta p_n and

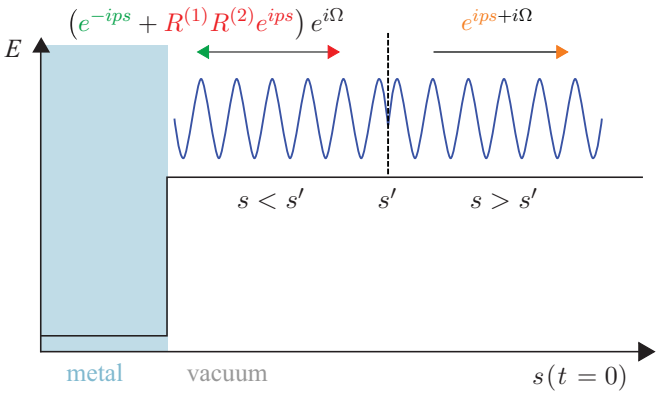

FIG. 1. (Color online) Sketch of the plane-wave components of the Green's function (perturbation at s'), taking into account a finite reflection amplitude at the metal-vacuum interface.

k_n on the upper and lower potential levels, respectively; $R_n^{(2)}$ represents the influence of the oscillatory field on the reflection, giving the amplitude of an elastic flip-flop transition.[50–52]

The reflection coefficients with (solid green) and without (dashed red) $R_n^{(2)}$ are shown in Fig. 2 for different field strengths as a function of momentum p_n, comparing them with a more involved (and slower) computation of field-dependent reflection coefficients in a Floquet method (dotted blue). Interestingly, the inclusion of $R_n^{(2)}$ gives a drastic improvement over the more simplified picture with only $R_n^{(1)}$ and deviates from the numerical approach only at very high fields [Fig. 2(d)], where reflection is suppressed in any case.

Three observations regarding Eq. (13) can be made. First, in the limit of the zero field, this approximation is compatible with the outgoing boundary condition in the metal (minus infinity). Second, while we approximately satisfy the boundary condition at minus infinity, we still have an exact solution of Eq. (6) at positive z. Thirdly, the proposed approximation goes beyond the strong-field approximation, because it incorporates the effect of a potential well. As we will show later,

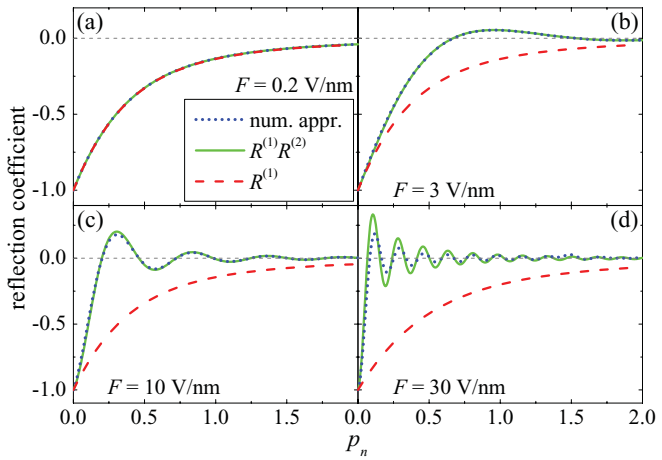

FIG. 2. (Color online) The reflection coefficients as functions of momentum p_n from analytical [dashed red: $R^{(1)}$ only; solid green: $R^{(1)}R^{(2)}$] and numerical (dotted blue) computations for different field strengths (a) $F = 0.2$ V/nm, (b) 3 V/nm, (c) 10 V/nm, and (d) 30 V/nm.

this approximation yields good quantitative agreement with numerical results of a direct integration of the Schrödinger equation.

B. Formula for photoemission probability

Having constructed the Green's function, we can now calculate the solution of Eq. (3) from the integral representation

$$\psi(z,t) = \psi_0(z,t) + \int_0^T \int_0^\infty G(z,t;z',t')V_F(z',t')\psi_0(z',t')dz'dt', \quad (16)$$

where $V_F(z,t) = -zeF\cos\omega t$. The momentum-dependent transmission probability $w(k)$ through a time-dependent triangular barrier is defined as the ratio of transmitted and incident current densities. After some algebra we obtain the following expression from Eq. (16):

$$w(k) = \sum_{n\geqslant N(k)} \frac{1}{kp_n}\left|\frac{1}{T}\int_0^T \langle\psi_{p_n}^{\mathrm{mV}}(z,t)|V_F|\psi_0(z,t)\rangle dt\right|^2, \quad (17)$$

where

$$\psi_{p_n}^{\mathrm{mV}*}(z,t) = \psi_{p_n}^{(-)}[s(z,t)]e^{-i\Omega_n(t,0)}, \quad (18)$$

and we sum over all open channels. $N(k)$ denotes the minimum number of photons necessary for the photoemission process, according to Eq. (10). The functions ψ_0, Ω_n, and $\psi_{p_n}^{(-)}(s)$ in Eq. (17) are given by Eqs. (2), (9), and (13), respectively. We employ the $\langle\cdots\rangle$ notation to represent the integration over the spatial variable $z\in[0,\infty)$. In an analogy with above-threshold ionization in atoms,[53–56] each term of the sum in Eq. (17) can be interpreted as an n-photon contribution:

$$w(k) = \sum_{n\geqslant N(k)} w_n(k). \quad (19)$$

The terms with n larger than $N(k)$ correspond to above-threshold photoemission channels. Furthermore, we have to sum over all occupied states of electrons in the metal, which leads to the total current emitted by a unit surface.

Equation (17) corresponds to the transition probability in a strong-field approximation,[23,28] except for the replacement of the final states for each n-photon transition amplitude. Instead of final Volkov states, we use the mixed Volkov states $\psi_{p_n}^{\mathrm{mV}}$, which are superpositions of waves with opposite momenta. These final states take into account the major contribution of rescattering on the potential well, which is especially important in the weak-field regime. Using the following properties of the initial states and the Volkov states,

$$V_F\psi_{p_n}^{\mathrm{V}*}(z,t) = \left\{-i\frac{\partial}{\partial t} - \frac{1}{2}[p_n + p_{\mathrm{cl}}(t)]^2\right\}\psi_{p_n}^{\mathrm{V}*}(z,t), \quad (20)$$

$$i\frac{\partial}{\partial t}\psi_0 = E\psi_0, \quad (21)$$

we can evaluate the matrix element in Eq. (17). Equation (20) follows from the time-dependent Schrödinger equation for Volkov wave functions, and Eq. (21) follows from the assumption of a stationary initial state. After some algebra, we obtain the following final formula for the emission probability:

$$w_n(k) = \frac{k}{\alpha^2+k^2}\frac{1}{p_n}\left|I_n(p_n) + R_n^{(1)}R_n^{(2)}\,I_n(-p_n)\right|^2, \quad (22)$$

where we introduced the integral

$$I_n(p) = \frac{1}{2\pi}\int_0^{2\pi}\left(i\alpha + p + \frac{eF}{\omega}\sin q\right)\exp[iS(q)]dq, \quad (23)$$

$$S(q) = nq - \frac{peF}{\omega^2}\cos q - \frac{e^2F^2}{8\omega^3}\sin 2q. \quad (24)$$

Equations (22) and (23) present the main result of this subsection. These formulas describe the simple picture of the photoemission process as consisting of two actions: first, the electron absorbs n photons and becomes free; the electron then scatters elastically on the potential well. This physical picture is supplemented by a very simple way to evaluate the integrals (see Appendix B).

III. TOTAL CURRENT DENSITY AND ANGULAR DISTRIBUTION OF EMITTED ELECTRONS

In the previous section, we derived expressions for the emission probability in the one-dimensional case. A number of experimentally observable quantities, such as the angular distribution of emitted electrons, require a three-dimensional treatment. Considering the translational symmetry parallel to the surface and the associated conservation of the parallel momenta k_x,k_y of the initial momentum $\vec{k} = (k_x,k_y,k_z)$, the results of the one-dimensional treatment also apply to a three-dimensional planar surface. For the corresponding three-dimensional expressions, the one-dimensional momentum k in Eq. (22) merely has to be replaced by the projection k_z related to the motion perpendicular to the surface.

Next, we employ the formula for the current incident on the metal surface of the unit area:[57,58]

$$J_0 = g\int\frac{d^3k}{(2\pi)^3}\frac{k_z}{e^{\beta[(k_x^2+k_y^2+k_z^2)/2-E_F]}+1}. \quad (25)$$

Here, $g=2$ is the spin multiplicity of the electron, β denotes the inverse thermal energy, and d^3k is the three-dimensional volume element in momentum space. The exponential in the integrand in Eq. (25) originates from the equilibrium Fermi-Dirac distribution.

By multiplication with the probability $w_n(k_z)$ of the n-photon process found in Sec. II B, an expression for the n-photon contribution of the total current emitted by a unit surface is obtained:

$$J = 2\int\frac{d^3k}{(2\pi)^3}\sum_{n\geqslant N(k_z)}\frac{k_z w_n(k_z)}{e^{\beta[(k_x^2+k_y^2+k_z^2)/2-E_F]}+1}. \quad (26)$$

Since k_x, k_y are conserved quantum numbers we may write

$$k_x = p_n\tan\theta\,\cos\varphi, \quad k_y = p_n\tan\theta\,\sin\varphi, \quad (27)$$

where p_n denotes the vector projection of the final momentum on the z axis and θ and φ are the polar and azimuthal angles of the final momentum, associated with a spherical coordinate system. Combining Eqs. (26) and (27) and using the formula

$$dk_xdk_y = \frac{p_n^2}{\cos^3\theta}d\Omega, \quad (28)$$

we obtain for the angular distribution of the total current

$$\frac{dJ}{d\Omega} = \frac{2}{(2\pi)^3}\frac{1}{\cos^3\theta}\int_0^\infty \sum_{n\geqslant N(k_z)} \frac{p_n^2 k_z w_n(k_z) dk_z}{e^{\beta[(k_z^2+p_n^2\tan^2\theta)/2-E_F]}+1}. \tag{29}$$

The angular distribution does not depend on the azimuthal angle φ because of the cylindrical symmetry of the problem. The total current emitted by a unit surface can be calculated by integration over the solid angle Ω. The integration yields

$$J = \int_0^\infty \sum_{n\geqslant N(k_z)} k_z w_n(k_z) F(k_z) dk_z, \tag{30}$$

where $F(k_z)$ is the momentum distribution of free electrons projected on the z axis:

$$F(k_z) = \frac{2}{(2\pi)^2}\frac{1}{\beta}\ln\left[1+e^{\beta(E_F-k_z^2/2)}\right]. \tag{31}$$

Similar expressions can also be obtained by using material-specific band structures and density of states. Furthermore, note that in an analogy with the generalized Fowler-DuBridge theory each term of the sum in Eq. (30) can be interpreted as a partial current.[22] In the low-temperature limit, we may write Eq. (29) as

$$\lim_{\beta\to\infty}\frac{dJ}{d\Omega} = \frac{1}{(2\pi)^3}\frac{1}{\cos^3\theta}\int_0^{k_{\max}(\theta)} \sum_{n\geqslant N(k_z)} p_n^2 k_z w_n(k_z) dk_z, \tag{32}$$

where the final momentum p_n is defined by Eq. (10), and the upper limit of the integration in Eq. (32) is given by the condition

$$\tfrac{1}{2}k_{\max}^2(\theta) = E_F - (n\omega - W - U_p)\sin^2\theta. \tag{33}$$

The upper integration limit in Eq. (32) follows from the exponential term in Eq. (29). Physically, the quantity $k_{\max}(\theta)$ is the angle-dependent perpendicular component of the momentum at the Fermi energy. Thus, it gives the maximum perpendicular momentum at any emission angle. Since the expression in brackets in Eq. (33) is positive for open channels, $k_{\max}(\theta)$ decreases with an increasing emission angle. Equations (29), (30), and (32) are the main results of this subsection.

IV. TUNNELING APPROXIMATION

In this section we use the perturbation theory to derive simplified expressions in the strong-field limit. It will be shown that in this regime the well-known tunneling formula is obtained.

For the photoemission process, the integral over phase in Eq. (23) contains a rapidly oscillating function $\exp[iS(q)]$, where $S(q)$ is the coordinate-independent part of the classical action, given by Eq. (24). This fact allows us to employ the saddle-point method,[27,59] which is known to work very well for sufficiently strong fields. First, we exclude n from Eq. (24) by using Eq. (10) and then introduce the effective frequency of the oscillations as

$$S'(q) = \frac{1}{2\omega}\left(p + \frac{eF}{\omega}\sin q\right)^2 + \frac{\alpha^2}{2\omega}. \tag{34}$$

The positions of the saddle points are given by the equation $S'(q) = 0$, which yields for the points in the upper complex half plane

$$\sin q = \frac{\omega}{eF}(i\alpha - p). \tag{35}$$

This equation has many solutions, but only one of them, the point approaching the maximum of the electric force $eF\cos(q)$ at $p = 0$, contributes to integral (23) at sufficiently strong fields. According to the general theory of adiabatic transitions,[60] this point can be interpreted as an "instant of emission."

For the second derivative we obtain

$$S''(q) = \frac{i\alpha F}{\omega^2}\cos q. \tag{36}$$

Now the integral, defined by Eq. (23), can be approximately calculated by the formula

$$I_n(p) = \frac{i\alpha}{\pi}\left[\frac{2\pi i}{S''(q)}\right]^{1/2}\exp[iS(q)], \tag{37}$$

where q is a suitable solution of Eq. (35). Combining Eq. (37) and the definition of $w(k)$ from Eq. (22), one obtains the expression for the total probability:

$$w(k) = \frac{2\omega}{\pi}\frac{\alpha k}{\alpha^2+k^2}\int_0^\infty \frac{1}{|F\cos q|}\exp[-2\mathrm{Im}\,S(q)]dp, \tag{38}$$

where the summation over n absorbed photons is carried out using

$$\sum_{n\geqslant N(k)} \upsilon(p_n) = \frac{1}{\omega}\int_0^\infty p\upsilon(p)dp. \tag{39}$$

Since q defined by Eq. (35) is a function of p, the integrand in Eq. (38) can be treated as a momentum distribution of the ejected electrons in the strong-field regime. An evaluation of Eq. (38) yields the total emission probability from a single energy level in the metal.

To obtain the tunneling approximation we propose the following analytic approximation for the imaginary part of the classical action $S(q)$:

$$\mathrm{Im}\,S(q) = \frac{\alpha^3}{3F}\left[1-\frac{1}{10}\left(\frac{\omega\alpha}{eF}\right)^2\right]\Big/\sqrt{1-\left(\frac{\omega p}{eF}\right)^2}. \tag{40}$$

Using a Taylor expansion over the field variable, it can be seen that in the strong-field limit, this expression correctly reproduces the explicit imaginary part of Eq. (24) up to F^{-3}.

We substitute Eq. (40) in Eq. (38) and introduce the variable of integration q_0 by the substitution

$$p = -\frac{eF}{\omega}\sin q_0. \tag{41}$$

The physical motivation for this substitution follows from the connection of the drift momentum p with the phase of emission q_0 in an electric field $eF\cos q$. The right-hand side of Eq. (41) then gives the drift momentum for zero initial velocity. Since $q_0 \in [\frac{1}{2}\pi,\pi]$ is a real variable, the substitution introduces also a maximum kinetic energy, which is the classical cutoff energy $2U_p$.[71–73]

Finally, we obtain the leading contribution to the total probability:

$$w(k) = \frac{1}{\pi}\frac{2\alpha k}{\alpha^2 + k^2}\int_{\pi/2}^{\pi} \exp\left(-\frac{2\alpha^3}{3|F\cos q_0|}\right) dq_0. \quad (42)$$

The exponential term in the integrand coincides with the known expression for the Wentzel-Kramers-Brillouin (WKB) approximation of the tunneling probability through a static triangular barrier:[61]

$$w(k) = \frac{4\alpha k}{\alpha^2 + k^2}\exp\left(-\frac{2\alpha^3}{3F}\right). \quad (43)$$

Thus, we have shown that the approach developed in Sec. II is consistent with the general idea that, for very high fields, the photoemission process can be described by a plain cycle averaging of the tunneling probability for stationary fields (the Fowler-Nordheim formula). Note however that a cycle averaging of Eq. (43) gives two times bigger values than Eq. (42). This discrepancy most likely arises from the fact that Eq. (43) was derived in Ref. 61 in a weak-field limit and tends to overestimate the explicit result at strong fields (see Fig. 3). Instead, our tunneling approximation was obtained for sufficiently strong laser fields. The total probability in Eq. (42) does not exceed 0.5 because the ejection of the electrons is possible only when the electric force $eF\cos q$ is positive.

In order to obtain the total current J emitted by a unit surface, we have to sum over all occupied electronic states in the metal, according to Sec. III. The leading contribution of the integration is given by

$$J = \frac{1}{16\pi^2}\sqrt{\frac{E_F}{W}}\frac{F^2}{W + E_F}\exp\left(-\frac{4\sqrt{2}W^{3/2}}{3F}\right), \quad (44)$$

where E_F denotes the Fermi energy and W is the work function of the metal. Equation (44) is similar to the known Fowler-Nordheim formula for the emission current density in the static electric field F.[61,62] Equations (38) and (42) are the main results of this subsection.

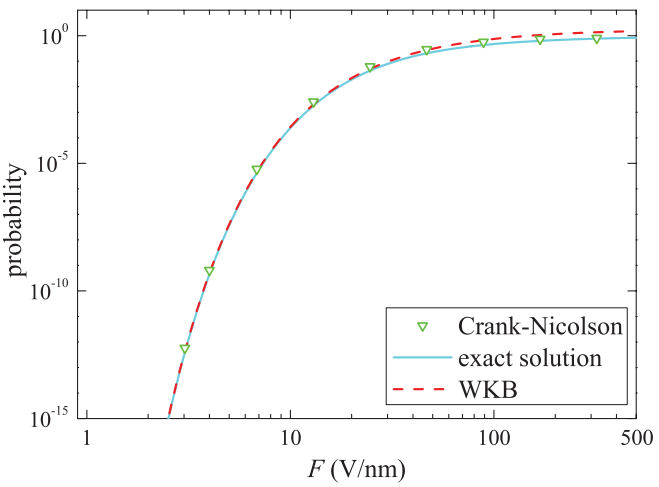

FIG. 3. (Color online) Tunneling probability for a triangular barrier as a function of the static electric field: exact result (cyan line), WKB approximation (red dashed line), and Crank-Nicolson scheme (triangles). Work function and Fermi energy are 5.5 and 4.5 eV, respectively.

V. VARIATIONAL FORMULATION OF FLOQUET METHOD

The method of matching wave functions at an interface joining two media with differing properties is widely used in quantum theory. Recently, this method was discussed within the context of a photoemission process.[30] Here, we present the variational version of this approach.

In order to employ the variational method for Eq. (3), we first introduce a trial solution satisfying the appropriate radiation conditions for this problem. For later convenience, we omit the phase factor $\exp(-iEt)$, where E is the energy of the initial state [cf. Eq. (2)]. The trial solution for negative z is given by

$$\psi^{(-)}(z,t) = \exp(ikz) + \sum_{n=-N_{\max}}^{N_{\max}} R_n \exp(-ik_n z - in\omega t). \quad (45)$$

The wave internally reflected from the surface contains both an elastic reflection and a superposition of waves with energies changed by integer multiples of the photon energy. The corresponding momenta of the reflected plane-wave components are given by $k_n = \sqrt{k^2 + 2n\omega}$ with initial momentum k, R_n denote the reflection amplitudes, and n is the number of absorbed photons. The minus superscript on $\psi^{(-)}$ indicates that the trial function solves Eq. (3) at negative z. For positive z, the trial function $\psi^{(+)}$ is given by the following linear combination of Volkov solutions:

$$\psi^{(+)}(z,t) = \sum_{n=-N_{\max}}^{N_{\max}} T_n \exp\left[i\left(p_n + \frac{eF}{\omega}\sin\omega t\right)z\right] \times \exp\left(\frac{ip_n eF}{\omega^2}\cos\omega t + \frac{ie^2F^2}{8\omega^3}\sin 2\omega t - in\omega t\right), \quad (46)$$

where p_n are the momenta of the transmitted modes, given by Eq. (10), and T_n are the transmission amplitudes. Next, we introduce the functional

$$I = \int_0^T [\psi^{(+)}(0,t) - \psi^{(-)}(0,t)]^2 dt + s\int_0^T \left[\frac{\partial\psi^{(+)}}{\partial z}(0,t) - \frac{\partial\psi^{(-)}}{\partial z}(0,t)\right]^2 dt, \quad (47)$$

where the parameter $s = k^{-2}$ in front of the second integral was introduced from dimensional considerations. The quantity I is then a function of R_n and T_n. The matching conditions, requiring both the wave function and its first derivative to be continuous at $z = 0$, are obtained by minimizing I with respect to each of these parameters. Selecting a sufficiently large number $N_{\max}$, we obtain an approximation very close to the exact matching conditions. Minimizing the functional yields the following system of linear equations:

$$\begin{aligned} \sum_{m=-N_{\max}}^{N_{\max}} \left(A^s_{nm}T_m + B^s_{nm}R_m\right) &= -B^{-s}_{n0}, \\ \sum_{m=-N_{\max}}^{N_{\max}} \left[\left(B^s_{mn}\right)^* T_m + D^s_{nm}R_m\right] &= -D^{-s}_{n0}. \end{aligned} \quad (48)$$

Formulas for the matrix elements A^s_{nm}, B^s_{nm}, and D^s_{nm} are given explicitly in Appendix C. Equations (48) allow us to determine the transmission amplitudes T_n and to subsequently calculate the photoemission probability as

$$w(k) = \sum_{n \geqslant N(k)} w_n(k), \quad w_n(k) = \frac{p_n}{k}|T_n|^2, \tag{49}$$

where $w_n(k)$ describes the n-photon contribution.

Note that, although our approach is also based on the matching condition and is therefore similar to the procedure implemented in Ref. 30, there is an important difference: we use the variational method rather than a Fourier expansion for time-periodic functions. According to the variational theorem, our approach guarantees the best approximation of the matching conditions for a given number $N_{\max}$.

Finally, the results of the Floquet approach also serve as a good approximation not only to continuous-wave excitation but also to time-varying or pulsed fields, as long as the optical frequency is much bigger than the bandwidth of the driving field. We will see in Sec. VII that the Floquet computations for a continuous-wave excitation are in quite good agreement with the results for 10-cycle pulses obtained within the Crank-Nicolson method [compare Figs. 4 and 7(b)].

VI. MODIFIED CRANK-NICOLSON SCHEME

Strictly speaking, the Floquet method is only applicable to continuous wave, i.e., time-periodic, fields. Nevertheless, it can be extended to consider pulses within the applicability of a slowly varying envelope approximation. For even shorter pulses, e.g., in the few-cycle range and to describe carrier-envelope effects, a direct integration of the Schrödinger equation is desirable. The Crank-Nicolson method is one numerical scheme for the integration of the Schrödinger equation and has been used for nonlinear photoemission from localized initial states.[63] Here, we present an extension of the numerical scheme, taking into account the delocalized nature of initial states, which has important consequences for the photoemission yield in the strong-field regime.

In the numerical implementation we will solve Eq. (3) for a bounded spatial domain $[a,b]$. A weak formulation of this problem is obtained by multiplying Eq. (3) with a so-called test function $\varphi(z) \in L^2[a,b]$ and integrating by parts:

$$\int_a^b \varphi\left(i\frac{\partial\psi}{\partial t} - V\psi\right)dz - \frac{1}{2}\int_a^b \frac{\partial\varphi}{\partial z}\frac{\partial\psi}{\partial z}dz + \frac{1}{2}\varphi\frac{\partial\psi}{\partial z}\Big|_a^b = 0, \tag{50}$$

where $\psi(z,t)$ is the solution of the time-dependent Schrödinger equation with the potential $V = V_W + V_F$ [Eq. (1)]. V_W denotes the potential well and $V_F = -zeF(t)\eta(z)$ is the induced time-dependent potential with the Heaviside function $\eta(z)$. We now focus on the derivation of a fully discrete approximation to Eq. (50). For this reason, we introduce the uniform time discretization $\psi^{(m)}(z) = \psi(z,t^{(m)})$, where $t^{(m)} = m\triangle t$, $m \in \mathbb{N}$ with time step size $\triangle t$. We use the implicit midpoint rule for the time derivative.

To treat the boundaries, transparent boundary conditions are imposed.[44,45] These boundary conditions are nonlocal in time and can formally be written in terms of a fractional time derivative, which is explicitly given in Ref. 44. However, it is more important for us that these boundary conditions can be written in the temporally discrete form

$$\frac{\partial\psi^{(m)}}{\partial z} = \frac{\partial\tilde{\psi}_0^{(m)}}{\partial z} \pm 2g\sum_{k=1}^{m}\beta_{m-k}\exp\{i[\mathcal{V}^{(k)} - \mathcal{V}^{(m)}]\}\left[\psi^{(k)} - \tilde{\psi}_0^{(k)}\right], \tag{51}$$

where plus and minus correspond to the right and left boundaries, respectively. The coefficients β_{m-k} are given explicitly in Ref. 45:

$$\beta_{2n} = \frac{(2n)!}{(2^n n!)^2}, \quad \beta_{2n+1} = -\beta_{2n}. \tag{52}$$

The $\mathcal{V}^{(m)}$ are given by

$$\mathcal{V}^{(m)} = V_W t^{(m)} + \mathcal{V}_F^{(m)}, \quad \mathcal{V}_F^{(m)} = \sum_{k=1}^{m} V_F^{(k)}\triangle t, \tag{53}$$

where $V_F^{(k)}$ is the temporally discrete representation of the induced potential V_F. Note that $\mathcal{V}^{(m)}$ and $\mathcal{V}_F^{(m)}$ in Eqs. (53) are still functions of the spatial variable z. The "dressed" initial state is given by $\tilde{\psi}_0^{(m)}(z) = \exp[-i\mathcal{V}_F^{(m)}]\psi_0^{(m)}(z)$, where $\psi_0^{(m)}(z)$ is the temporally discrete representation of the initial state given by Eq. (2). The constant g is defined as

$$g = -\frac{1}{\sqrt{\triangle t}}\exp\left(-\frac{i\pi}{4}\right). \tag{54}$$

Substituting the spatial derivative $\psi_z^{(m)}$ from Eq. (51) in Eq. (50), we obtain the weak formulation in the presence of the boundary conditions. To obtain a fully discrete formulation of our problem, we follow the Petrov-Galerkin method[64] and employ the expansion

$$\psi^{(m)}(z) = \sum_{j=1}^{N} c_j^{(m)}\varphi_j(z), \tag{55}$$

where $\varphi_j(z)$ denote the basis functions, which are chosen as cubic B-splines with compact support. The elements $c_j^{(m)}$ are the fully discrete approximations to the exact solution of Eq. (3). Finally, the fully discrete approximation to Eq. (50) is written as

$$(\mathbf{I} - \mathbf{H}^{(m+1)})c^{(m+1)} = (\mathbf{I} + \mathbf{H}^{(m)})c^{(m)} + b^{(m)} + b^{(m+1)}, \tag{56}$$

where the column vector $c^{(m)}$ is defined by the elements $c_j^{(m)}$. The square matrix $\mathbf{H}^{(m)}$ in Eq. (56) is described by

$$H_{ij}^{(m)} = \frac{1}{2}\int_a^b \frac{d\varphi_i}{dz}\frac{d\varphi_j}{dz}dz + \int_a^b \varphi_i V^{(m)}(z)\varphi_j dz - g\varphi_i\varphi_j\Big|_{z=a} - g\varphi_i\varphi_j\Big|_{z=b}, \tag{57}$$

and the overlap matrix $\mathbf{I}$ originating from nonorthogonal basis functions is given by

$$I_{ij} = \frac{2i}{\triangle t}\int_a^b \varphi_i\varphi_j dz. \tag{58}$$

Note that the difference between the presented numerical scheme and the Crank-Nicolson scheme from Ref. 65 originates from the column vectors $b^{(m)}$ on the right side of Eq. (56). These vectors are defined by the elements

$$b_j^{(m)} = -\frac{1}{2}\varphi_j\left(\frac{\partial\psi^{(m)}}{\partial z} \mp 2g\psi^{(m)}\right)\Bigg|_a^b, \tag{59}$$

where the spatial derivative should be taken from Eq. (51).

The time iteration is performed in two steps. First, we evaluate the right part of Eq. (56). This is simply a matrix vector multiplication and a sum with the vectors $b^{(m)}$ and $b^{(m+1)}$, which includes boundary effects. The second step requires solving a linear system of equations involving the matrix Hamiltonian $\mathbf{H}^{(m)}$ with the time-dependent potential given by Eq. (1). This is the main computational difficulty. Inasmuch as the spatial discretization based on B-splines yields banded matrices with bands close to the main diagonal, this difficulty can be efficiently solved by direct methods.[66] For instance, the numerical procedure used here is based on a factorization into lower and upper triangular sparse matrices (LU factorization routine).

Although the approach involves computational difficulties, it has been proven that this scheme is unconditionally stable.[67] Thus, it can be successfully used for the determination of important physical properties related to photoemission by ultrashort laser pulses from an initially delocalized state, given by Eq. (2).

A good reference check for the numerical accuracy of the developed Crank-Nicolson variant is obtained by calculating the emission probability for a static electric field. Figure 3 shows the tunneling current through a static barrier as a function of applied field strength. Except for very strong fields, the WKB approximation given by Eq. (43), and an exact solution based on Airy functions [see, for instance Eq. (20) in Ref. 68] give very similar results for a wide range of field values. Truncation errors (from the double precision used numerically) are only encountered at emission probabilities below 10^{-15} (not shown).

VII. NUMERICAL RESULTS AND DISCUSSION

A. Yield dependence of different models

In order to assess the developed methodology, we compare the results derived in the different approaches.

In Fig. 4, we present the results for surface photoemission derived obtained with our Crank-Nicolson calculations (solid green), perturbation theory (dotted orange), and the Floquet method (dot-dashed and dashed blue). The excitation wave length was chosen as 800 nm, corresponding to a photon energy of $\hbar\omega = 1.55$ eV. The Fermi energy and the work function were taken to be 4.5 and 5.5 eV, respectively. Similar to the case of multiphoton ionization of atoms by an intense light field, the photoemission from metals is usually characterized by the Keldysh parameter $\gamma = \sqrt{W/2U_p}$.[26,69] Figure 4 illustrates the transition between the perturbative ($\gamma > 1$) and the tunneling regimes ($\gamma < 1$). For the transition region ($\gamma \approx 1$), one finds $F \approx 18$ V/nm. This transition from multiphoton to tunneling emission was observed experimentally on metal nanotips by Bormann *et al.*[15] The oscillatory

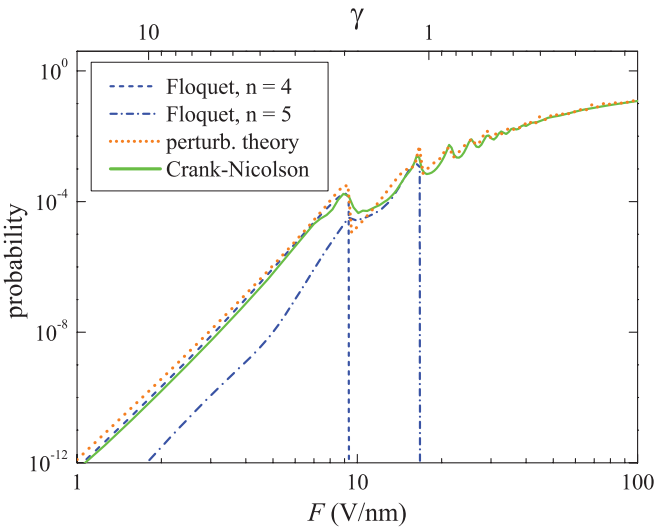

FIG. 4. (Color online) Emission probability, defined as the ratio of (time-averaged) outgoing and incoming current densities, as a function of the peak electric field of the incident light: results of continuous-wave Crank-Nicolson computations with the delocalized initial-state (solid green) and perturbative approach [Eq. (22)] (dotted orange). Results of the variational approach showing the contributions from four-photon (dashed blue) and five-photon (dot-dashed blue) absorption. Work function and initial-state energy (Fermi energy) are 5.5 and 4.5 eV, respectively.

structure in Fig. 4 can be explained by channel closing effects of different multiphoton orders,[28] close to fields where $p = 0$ in Eq. (10). The emission probabilities computed within the Crank-Nicolson and perturbative approaches show rather good agreement, except for a small deviation at the closing of the lowest-order channel ($n = 4$).

The two lowest individual channel contributions derived from the variational approach based on matching conditions (Floquet method) are shown as blue lines in Fig. 4. The predominant contribution in the weak-field regime stems from four-photon absorption, consistent with the work function and photon energy used. Also, this approach gives very good agreement with the other two methods. However, it should be noted that the Floquet method becomes less stable at larger field strengths, so its recommended use is primarily in the weak- and intermediate-field regimes, where it yields excellent results. We conclude that all three approaches are generally very accurate for continuous-wave excitation. Using a slowly varying envelope approximation, the results for the Floquet method and the perturbation theory can be extended to pulsed excitation in a straightforward way,[15] while the Crank-Nicolson approach is of course valid for all time-varying fields.

B. Surface current: Crank-Nicolson approach

To obtain some additional insight, we use the adapted Crank-Nicolson scheme to calculate the time-resolved current through a metal surface illuminated by a continuous wave, shown in Fig. 5. As shown in Fig. 5(b), the maximum of the surface current is found at $\omega t \approx \pi/2$ in the weak-field regime ($\gamma > 1$); i.e., the driving field and surface current are out of phase. The maximum surface current is approximately

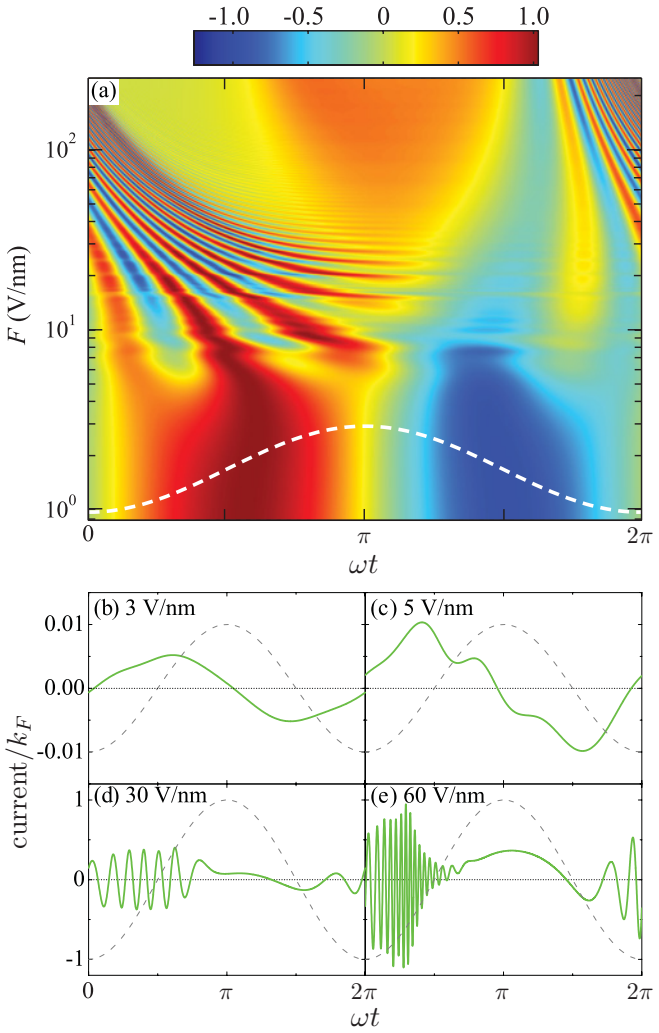

FIG. 5. (Color online) (a) Normalized time-resolved surface current as a function of both the peak electric field and temporal coordinate. Dashed line indicates electric force. Work function and Fermi energy are 5.5 and 4.5 eV, respectively. Lower panel: exemplary curves for Keldysh parameters (b) $\gamma = 6$, (c) $\gamma = 3.6$, (d) $\gamma = 0.6$, and (e) $\gamma = 0.3$.

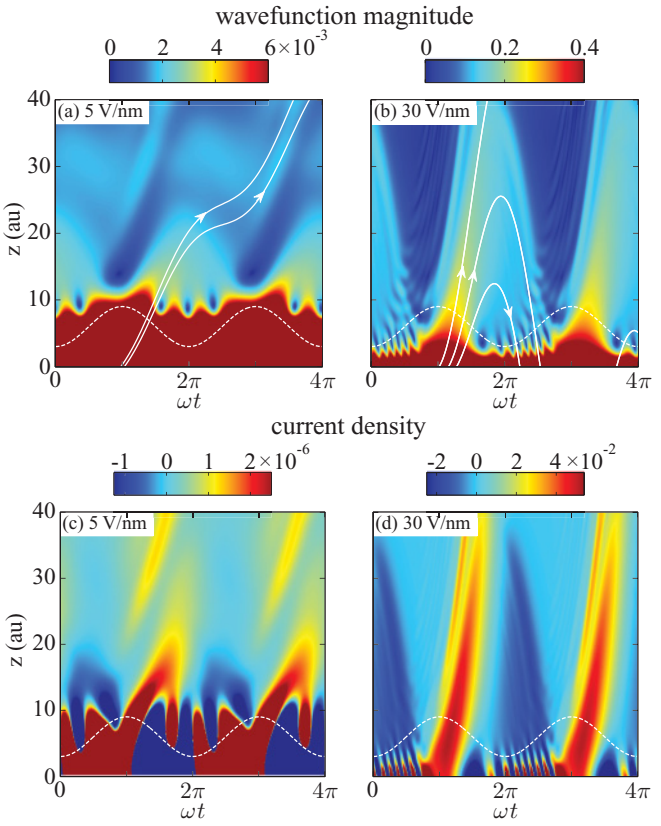

FIG. 6. (Color online) Magnitude of [(a), (b)] wave function $|\psi(z,t)|$ and [(c), (d)] current density as a function of time and space. Dashed lines indicate electric force for reference. Solid white lines show corresponding classical trajectories. Parameters: $W = 5.5$ eV and $E_F = 4.5$ eV.

$10^{-2}k_F$, while the averaged emission current, as seen in Fig. 4, is only about $10^{-8}k_F$. This indicates that the vast majority of electrons transiently excited near the surface are not emitted. This situation changes dramatically with increasing field strength [cf. Fig. 5(e)]. Here, the instantaneous surface current becomes rapidly oscillating, except for $\omega t \approx \pi$. Thus, the major contribution to the time-averaged current is generated in phase with the driving force. Also, the maximum emission current and the corresponding averaged current in Fig. 4 are of the same order of magnitude. The time-dependence of the emission current and its relative phase to the driving force should be relevant for the application and interpretation of nonlinear photoemission in the detection of carrier envelope phases.[63,70] Figure 5(a) provides a more complete illustration of the transition between the weak-field and strong-field regimes, in which also the channel closings are apparent as weak horizontal features.

In order to study the photocurrent in more detail, we plot the space and time dependence of the absolute value of the computed wave function $|\psi(z,t)|$ in Figs. 6(a) and 6(b) and the instantaneous current density in Figs. 6(c) and 6(d). Here, the time axis covers two optical cycles, and the spatial domain shows the vacuum region with the metal surface at $z = 0$. Figures 6(a) and 6(b) can be formally split into two regions: a near region ($z < 10$ a.u.) and a far region ($z > 10$ a.u.). In the near region, the exponential tail of the initial state mainly undergoes oscillations in phase with the electric force $eF\cos\omega t$, schematically represented by the dashed line. These oscillations can be described in terms of a simple harmonic oscillator picture with its resonance frequency being the work function and the system driven at a much lower frequency (below resonance). At low field strength, and because the driving frequency is substantially lower than the work function, the state bound to the metal oscillates in phase with the driving force. The surface current corresponds to a time derivative of this wobble motion and results in the antisymmetric curve shown in Figs. 5(b) and 5(c).

At higher field strengths, this symmetry is broken, because the surface current no longer consists mostly of wobble motion but contains a substantial contribution from the tunnel current, which has its maximum at the phase of maximum of the driving force, i.e., at $\omega t = \pi$. For comparison, the solid white lines

show the corresponding classical motion.[71–73] For a cosine electric field, the classical trajectories are given by

$$z(t) = \left(v_0 - \frac{eF}{\omega}\sin\omega t_0\right)(t - t_0) + \frac{eF}{\omega^2}(\cos\omega t_0 - \cos\omega t), \tag{60}$$

where the first brackets contain the drift momentum, v_0 denotes the initial velocity, and t_0 is the time of emission. It is usually assumed that the electron is born around the maximum of the electric force with zero initial velocity. However, in comparing classical trajectories with the quantum mechanically computed probability densities, we have found that much better agreement in the weak-field regime is obtained for a small positive velocity $v_0 < \sqrt{2\omega}$. The small initial velocity v_0 is obviously the result of excess energy in the quantum mechanical transition, which becomes a less important contribution at strong fields. Because of the initial nonzero velocity, in contrast to the usual treatment, classical trajectories starting even slightly after the maximum of the electric force escape the surface, while later trajectories return to and scatter at the surface. The fast oscillations in the near region [shown in Figs. 5(d), 5(e), and 6(d)] thus stem from the interference of various wave-function components, consisting of the initial state, emitted, returning, and rescattered amplitudes. The frequency of the oscillations increases with the field strength due to the additional kinetic energy accumulated in the far region. The maximum kinetic energy of returning electrons for $v_0 = 0$ is well known as approximately $3.2U_p$.[71] Figure 6(d) also shows that the rescattered amplitude back into the vacuum is relatively small.

C. Pulsed excitation: Crank-Nicolson approach

In the following, we apply the modified Crank-Nicolson scheme to evaluate the surface photoemission probability by short and ultrashort pulses, using the same parameters as before (with Fermi energy $E_F = 4.5$ eV and work function $W = 5.5$ eV). We study the emitted charge as a function of the peak field strength for a Gaussian pulse of the form $F(t) = -F_0 e^{-2\ln 2(t/\tau)^2}\cos\omega t$, where F_0 is the peak field strength and τ denotes the full width at half maximum of the intensity envelope. Symmetric pulses are assumed throughout this paper. An analysis of carrier-envelope effects will be the subject of future study.

Figure 7 displays the emitted charge (normalized to the pulse duration τ) for incident pulse lengths between one and ten optical cycles at a center wavelength of 800 nm, corresponding to durations between 2.7 and 27 fs. Generally, similar yield dependencies on the incident field strength as in continuous-wave excitation are observed (cf. Fig. 4), which also justifies the use of the perturbation theory for moderate pulse lengths. Modifications mainly appear in a decrease of the oscillatory structure near the channel closings, which becomes increasingly evident for shorter pulse durations. The two effects responsible for this observation are: (i) the continuous distribution of field strengths within the pulse envelope and, more importantly, (ii) the finite frequency bandwidth in pulsed excitation, which causes channel closings at different spectral components to occur at different peak field strengths.

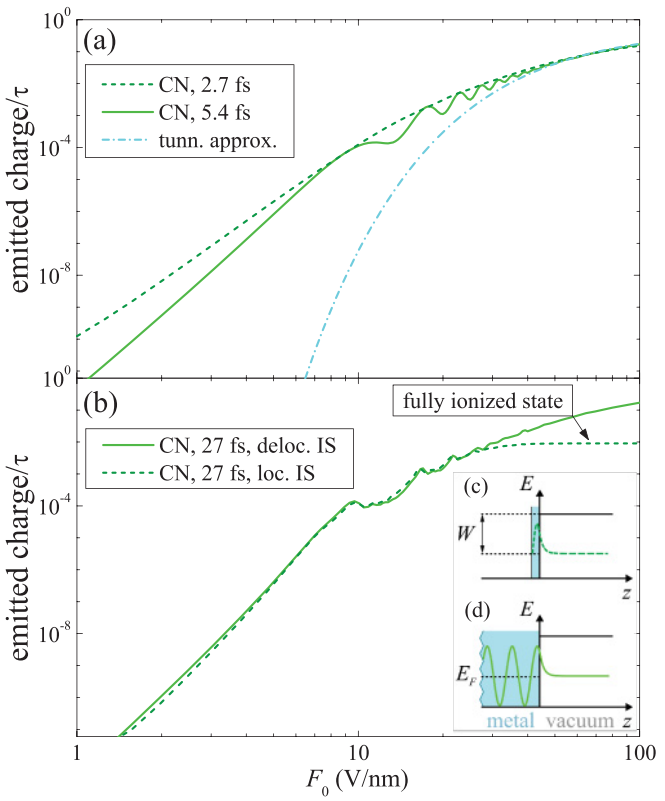

FIG. 7. (Color online) (a) Crank-Nicolson computations for photoemission as a function of the peak electric field F_0 for single- (dashed) and two-cycle (solid) pulses and tunneling approximation (dot-dashed cyan). (b) Comparison of Crank-Nicolson photoemission yield for localized (dashed) and delocalized (solid) initial-state computations (the dashed curve is fit to agree with the solid curve for weak fields). The inset schematically depicts the metal-vacuum interface (spatial coordinate $z = 0$) for (c) localized and (d) delocalized initial states.

In the strong-field regime, the charge emitted from the Fermi level is proportional to the pulse duration and can be estimated as $k_F w(k_F)\tau$, where k_F denotes the Fermi momentum and $w(k_F)$ is the tunneling probability (at the Fermi level) given by Eq. (42) for a continuous wave. The Crank-Nicolson computations approach this limit for large field strengths [cyan line in Fig. 7(a)].

In Figure 7(b), the emitted charges from localized (dashed) and delocalized (solid) initial states are compared for incident ten-cycle pulses. It is evident that deviations occur at field strengths beyond a Keldysh parameter of unity (corresponding to a field of 18 V/nm), where depletion of the localized initial state results in a current saturation.

D. Angular distribution: perturbation theory

A particular advantage of the perturbative approach developed in Sec. II is its straightforward extension from a one-dimensional formulation to a problem in which the angular emission characteristics in three-dimensional-space can be described (Sec. III). We now discuss the results of these computations. The polar plot in Fig. 8 displays the angular distributions for different Keldysh parameters,

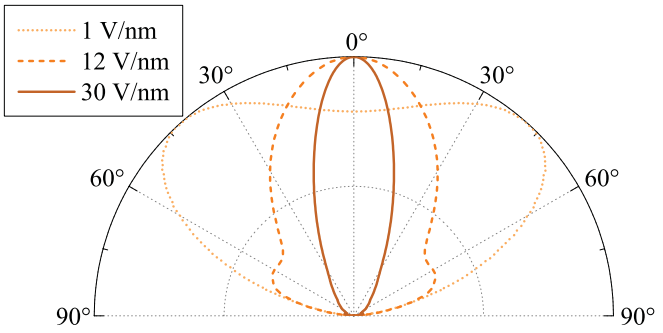

FIG. 8. (Color online) Normalized angular distributions of emitted electrons in the low-temperature limit [Eq. (32)] for field strengths of $F = 1$ V/nm ($\gamma = 18$, dotted), $F = 12$ V/nm ($\gamma = 1.5$, dashed), and $F = 30$ V/nm ($\gamma = 0.6$, solid), derived from perturbation theory. The angles denote the emission direction perpendicular to the metal surface.

each normalized to the angular maximum. The simulation parameters are the same as previously.

In the weak-field regime, a relatively broad emission cone with an opening angle of about 60° is found (dotted), which narrows substantially for increasing field strengths (dashed and solid), down to approximately 15° at $\gamma = 0.6$. Angular oscillations at weak and intermediate fields stem from the oscillatory dependence of the emission probability on the initial energy, which, via Eq. (33), couples to the total angular current. A rather narrow emission cone at strong light fields was also theoretically predicted in Ref. 74, as well as solid angle reduction in large static fields.[75] Experimentally, we have previously found a reduction in the solid angle of emission from metal nanotips in the transition from the weak- to the strong-field regime.[15] In that experiment, the emission was induced from a highly curved surface, whereas Eq. (32) is derived for a flat surface. This explains why the solid angle reduction in the experiment was less pronounced. Quantitative agreement with the experimental data could be obtained by integrating the local current density over the curved surface.[76,77]

E. Effective nonlinearity: Floquet method and perturbation theory

While the Crank-Nicolson approach can be considered as being the most versatile, the computations within the Floquet method discussed below are appealing because of their numerical simplicity and accuracy for weak and intermediate fields. Figures 9(a) and 9(b) show double logarithmic plots of the total emission yield as well as the four- and five-photon contributions for work functions of $W = 5.2$ and 5.5 eV, respectively. In both cases, the threshold multiphoton process is four-photon photoemission, so that from conventional multiphoton descriptions (e.g., Fowler-DuBridge-type generalizations) an effective nonlinearity of 4 is expected throughout the weak-field regime, and the emission probability is assumed to scale with the fourth power of the intensity ($\propto F^2$). However, the present theoretical treatment shows that the effective nonlinearity—even at fields for which the four-photon contribution is dominant—may substantially differ

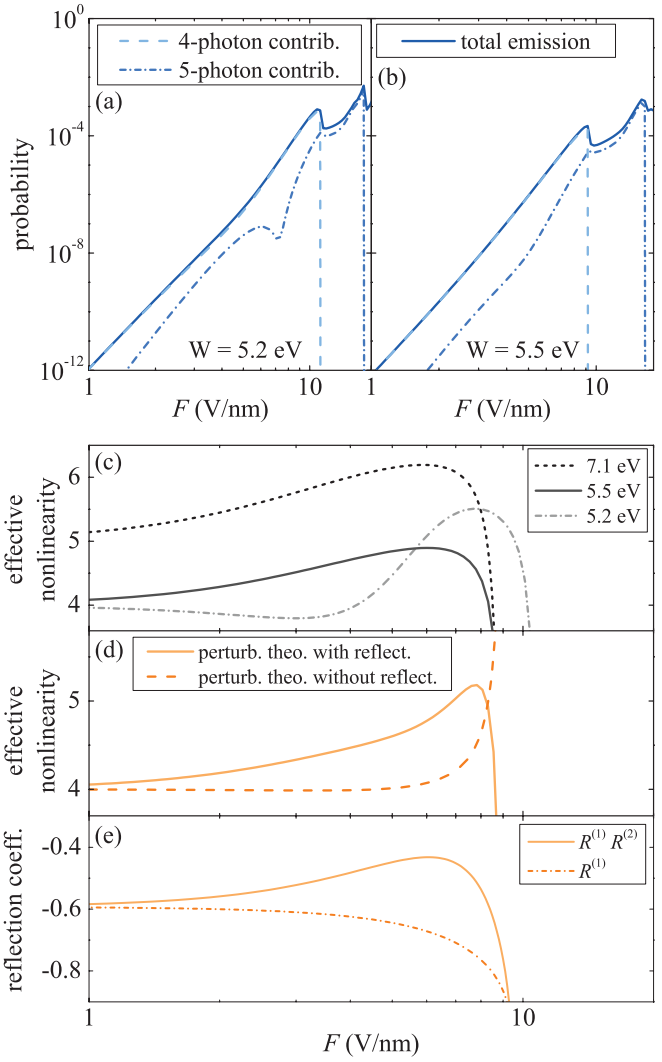

FIG. 9. (Color online) (a)–(c) Emission probability and effective nonlinearity computed with the Floquet method. Four-photon contribution (dashed), five-photon contribution (dot-dashed), and total emission probability (solid) for work functions of (a) $W = 5.2$ eV and (b) $W = 5.5$ eV. (c) Effective nonlinearity for $W = 5.2$ eV (dot-dashed), $W = 5.5$ eV (solid), and $W = 7.1$ eV (dashed). (d)–(e) perturbation-theory computations, illustrating the role of reflection in the enhancement of the effective nonlinearity ($W = 5.5$ eV). (d) Effective nonlinearity with (solid) and without (dashed) inclusion of surface reflection. (e) Field-dependent reflection coefficients (four-photon process) from Eqs. (14).

from the value of 4, is dependent on field strength, and is highly sensitive to the work function.

Figure 9(c) displays the effective nonlinearity of the photoemission process as a function of the field strength. Note that while the photoemission yields are plotted as a function of field throughout this paper, the effective nonlinearity refers to a power-law scaling of the current with the intensity. At a work function of 5.2 eV, the effective nonlinearity remains close to four up to fields of 4 V/nm (dash-dotted), before it increases to a value above five and subsequently drops (near a local maximum of the yield). At a work function of 5.5 eV, a similar but more gradual slope variation is observed (dashed). Virtually the same behavior is found also for higher work

functions (and multiphoton orders), as evident from the curve for $W = 7.1$ eV (solid), for which the dependency is simply shifted up by the energy of one photon.

The affine nature of the curves for $W = 5.5$ eV (and the four-photon process) and 7.1 eV (and the five-photon process) suggests that the nonlinearity enhancement effect is related to the field-dependent momentum, which is identical in these two cases. A quantity directly connected to the momentum is the reflection coefficient (cf. Fig. 2), so that one may presume that surface reflection is responsible for the nonlinearity enhancement. In order to investigate this hypothesis, we perform computations in the perturbative approach because (in contrast to the Floquet method) it allows for the selective inclusion or exclusion of surface reflection. Figure 9(d) shows the effective nonlinearity obtained from these computations, both with (solid) and without (dashed) surface reflection. Despite small deviations from the corresponding Floquet calculations, it is apparent that the nonlinearity enhancement is only pronounced in the presence of surface reflection. In the absence of reflection, the effective nonlinearity stays nearly constant at a value of 4, except for a singularity very close to the channel closing, which is intrinsic to the perturbative approach [cf. Eq. (17)]. The origin of this behavior is found by plotting the field-dependent reflection coefficient [Fig. 9(e)]. The reflection coefficient $R^{(1)}R^{(2)}$ (solid), which is negative throughout the range, varies slowly at low fields, then decreases in magnitude, before it approaches -1 at the channel closing. The reduced surface reflectivity at fields of several volts per nanometer, caused by elastic flip-flop transitions, leads to an additional growth of the transition probability with intensity, compared with the bare four-photon scaling, and thus enhances the observed effective nonlinearity. For comparison, also the bare reflection coefficient $R^{(1)}$ excluding elastic flip-flop transitions is plotted (dash-dotted), which shows a monotonic behavior.

To reiterate, the effective nonlinearity of multiphoton photoemission need not scale with the respective order, even at field strengths where only the lowest-order channel contributes to the emission. It should be noted that deviations from the expected nonlinearity have been frequently observed experimentally,[15,78–81] for example in the context of strong-field photoemission from metal nanotips.[15] To our knowledge, such slope variations are still not fully understood. In some cases, the effect was qualitatively explained by electron gas heating in the metal.[78,82] The calculations presented in Fig. 9 suggest field-dependent reflection as an alternative explanation of the modified effective nonlinearity under certain conditions.

VIII. CONCLUSION

In this paper, we have theoretically treated multiphoton and strong-field photoelectron emission from a metal surface. Suitable analytical approximations and efficient numerical schemes were developed, focusing on surface-specific aspects. For example, in perturbation theory surface reflection was incorporated via a new Green's function, which describes the photoemission final state as a linear combination of Volkov states. To this end, an analytical approximation to the reflection coefficient in the presence of large fields is presented. We believe that the procedures and numerical evaluations should be readily applicable by others. The results obtained within the perturbative and Floquet approximations demonstrate very good agreement with more sophisticated numerical computations within a Crank-Nicolson method.

The computations have shown that the employed variational version of the Floquet method, being very effective at weak fields, becomes less accurate in the strong-field regime, because it requires the inclusion of many channels and quadruple precision in the calculations. This observation agrees with the results of Faisal *et al.*[30] In contrast, both the perturbative approach and the Crank-Nicolson scheme presented here demonstrate very high efficiency in the weak-field and strong-field regimes and in the transition region.

We have found that in the weak-field regime the effective nonlinearity of (threshold) multiphoton processes may be substantially larger than the expected value in Fowler-DuBridge-type generalizations, based on the ratio of work function and photon energy. The behavior, which strongly depends on the work function, is caused by surface reflection of the final state. We believe that this finding provides an explanation for frequently observed enhanced nonlinearities in experimental multiphoton emission. Finally, the theory considered in this paper also reproduces the experimentally found reduction of the solid angle of photoemission with increasing field strength.

In the present discussion, we have not considered the image potential in any of the treatments, in order to demonstrate the good correspondence between various computational models. In the Crank-Nicolson scheme, the image potential is easily implemented, and this will be considered in the future. Also the effects of field penetration into the metal may be included, although nonlinear bulk absorption will be greatly suppressed for metals with high reflectivity. Moreover, the presented approaches also allow for the extraction of a number of additional physical dependencies such as carrier envelope effects, wavelength dependencies, and kinetic energy spectra.

ACKNOWLEDGMENTS

We thank Xavier Antoine for fruitful discussions about transparent boundary conditions. S. V. Yalunin has been supported by the European Commission through the Erasmus Mundus program. Financial support by the Deutsche Forschungsgemeinschaft (DFG-ZUK 45/1 and SPP 1391) is gratefully acknowledged.

APPENDIX A: PROOF OF Eq. (7) FOR G^{SFA}

One may simply substitute G^{SFA} from Eq. (7) in the Schrödinger Equation (3) to verify that it is indeed a proper solution at positive z,z'. Substituting and using Eqs. (5), (8), and (9) we obtain

$$\left(i\frac{\partial}{\partial t}+\frac{1}{2}\frac{\partial^2}{\partial z^2}+zeF\cos\omega t\right)G^{\mathrm{SFA}} = \frac{1}{T}\sum_{n\in\mathbb{Z}}\exp[i\Omega(t,t')]\delta[s(z,t)-s(z',t')]. \quad \text{(A1)}$$

Noting from Eq. (9) and Eq. (10) that

$$\Omega_n(t,t') = zp_{\mathrm{cl}}(t) - z'p_{\mathrm{cl}}(t') + (U_p - E - n\omega)(t-t')$$

$$-\frac{1}{2}\int_{t'}^{t} p_{\rm cl}^2(\tau)d\tau, \tag{A2}$$

and using the identity

$$\sum_{n\in\mathbb{Z}}\frac{1}{T}\exp[i\omega n(t-t')] = \delta_p(t-t'), \tag{A3}$$

we obtain finally

$$\frac{1}{T}\sum_{n\in\mathbb{Z}}\exp[i\Omega_n(t,t')]\delta[s(z,t)-s(z',t')] = \delta(z-z')\delta_p(t-t'). \tag{A4}$$

APPENDIX B: NUMERICAL INTEGRATION OF RAPIDLY OSCILLATING FUNCTIONS

Here we describe the numerical procedure used in the paper for calculating the integral

$$I = \frac{1}{2\pi}\int_0^{2\pi} g(q)\exp[iS(q)]dq. \tag{B1}$$

Let us assume that this integral contains a slowly varying function $g(q)$ and a rapidly oscillating one $\exp[iS(q)]$. In order to evaluate this integral, we first divide the interval of integration into several smaller subintervals with the central points q_m and expand $S(q)$ in a Taylor series:

$$S(q) \approx S(q_m) + S'(q_m)(q-q_m). \tag{B2}$$

Using Eq. (B2) and the identity

$$\int_{q_m-h}^{q_m+h}\exp[iS'(q_m)(q-q_m)] = 2\frac{\sin[S'(q_m)h]}{S'(q_m)}, \tag{B3}$$

we can approximately compute the integral, defined by Eq. (B1), applying the N-point quadrature formula

$$I = \sum_{m=1}^{N} g(q_m)\exp[iS(q_m)]\frac{\sin[\pi S'(q_m)/N]}{\pi S'(q_m)}. \tag{B4}$$

APPENDIX C: FORMULAS FOR MATRIX ELEMENTS IN EQS. (48)

In the applications presented in this paper we solve Eqs. (48) numerically to evaluate the photoemission probability. Here, we present formulas for the matrix elements in Eqs. (48) in a form suitable for numerical evaluation.

The matrix elements $D^s_{nm} = D^s_{nn}\delta_{nm}$, where $D^s_{nn} = 1 + s|k_n|^2$. The matrix elements A^s_{nm} are expressed in terms of Bessel functions of integer order as

$$\begin{aligned} A^s_{nm} = i^{m-n}\Big\{ & sU_p[J_{m-n+2}(a) + J_{m-n-2}(a)] \\ & - \frac{seF}{2\omega}(p_m + p_n^*)[J_{m-n+1}(a) + J_{m-n-1}(a)] \\ & + (1 + sp_n^* p_m + 2sU_p)J_{m-n}(a)\Big\}, \end{aligned} \tag{C1}$$

where U_p denotes the ponderomotive potential [Eq. (11)], and

$$a = \frac{eF}{\omega^2}(p_m - p_n^*). \tag{C2}$$

The elements B^s_{nm} are given by the formula

$$\begin{aligned} B^s_{nm} = -\frac{1}{2\pi}\int_0^{2\pi}\left[1 - sk_m\left(p_n^* + \frac{eF}{\omega}\sin q\right)\right] \\ \times \exp\left[i(n-m)q - \frac{ip_n^* eF}{\omega^2}\cos q - \frac{ie^2F^2}{8\omega^3}\sin 2q\right]dq. \end{aligned} \tag{C3}$$

This integral can be numerically evaluated as was described in Appendix B. Note in conclusion that the elements B^s_{nm} can be alternatively expressed also in terms of generalized Bessel functions.

*yalunin@bk.ru
†cropers@gwdg.de

[1] F. Krausz and M. Ivanov, Rev. Mod. Phys. **81**, 163 (2009).
[2] D. von der Linde and K. Rzàzewski, Appl. Phys. B **63**, 499 (1996).
[3] J. S. Kim *et al.*, Science **321**, 1472 (2008).
[4] M. Aeschlimann, C. A. Schmuttenmaer, H. E. Elsayed-Ali, R. J. D. Miller, J. Cao, Y. Gao, and D. A. Mantell, J. Chem. Phys. **102**, 8606 (1995).
[5] F. Banfi, C. Giannetti, G. Ferrini, G. Galimberti, S. Pagliara, D. Fausti, and F. Parmigiani, Phys. Rev. Lett. **94**, 037601 (2005).
[6] F. Bisio, M. Nývlt, J. Franta, H. Petek, and J. Kirschner, Phys. Rev. Lett. **96**, 087601 (2006).
[7] W. S. Fann, R. Storz, and J. Bokor, Phys. Rev. B **44**, 10980 (1991).
[8] G. Farkas, A. Kohazi-Kis, and C. Tóth, Opt. Eng. **32**, 2476 (1993).
[9] S. Luan, R. Hippler, H. Schwier, and H. O. Lutz, Europhys. Lett. **9**, 489 (1989).
[10] P. Dombi *et al.*, Opt. Express **18**, 24206 (2010).
[11] P. Hommelhoff, Y. Sortais, A. Aghajani-Talesh, and M. A. Kasevich, Phys. Rev. Lett. **96**, 077401 (2006).
[12] C. Ropers, D. R. Solli, C. P. Schulz, C. Lienau, and T. Elsaesser, Phys. Rev. Lett. **98**, 043907 (2007).
[13] B. Barwick, C. Corder, J. Strohaber, N. Chandler-Smith, C. Uiterwaal, and H. Batelaan, New J. Phys. **9**, 142 (2007).
[14] S. A. Hilbert, A. Neukirch, C. Uiterwaal, and H. Batelaan, J. Phys. B **42**, 141001 (2009).
[15] R. Bormann, M. Gulde, A. Weismann, S. V. Yalunin, and C. Ropers, Phys. Rev. Lett. **105**, 147601 (2010).
[16] M. Schenk, M. Krüger, and P. Hommelhoff, Phys. Rev. Lett. **105**, 257601 (2010).
[17] W. E. Spicer, Phys. Rev. **112**, 114 (1958).
[18] C. N. Berglund and W. E. Spicer, Phys. Rev. **136**, 1030 (1964).
[19] G. D. Mahan, Phys. Rev. B **2**, 4334 (1970).

[20]J. H. Bechtel, W. L. Smith, and N. Bloembergen, Opt. Commun. **13**, 56 (1975).
[21]L. A. DuBridge, Phys. Rev. **43**, 727 (1933).
[22]G. Ferrini, F. Banfi, C. Giannetti, and F. Parmigiani, Nucl. Instrum. Methods Phys. Res., Sect. A **601**, 123 (2009).
[23]L. V. Keldysh, Sov. Phys. JETP **20**, 1307 (1965).
[24]A. M. Perelomov, V. S. Popov, and M. V. Terentev, Sov. Phys. JETP **23**, 924 (1966).
[25]F. H. M. Faisal, J. Phys. B **6**, L89 (1973).
[26]F. V. Bunkin and M. V. Fedorov, Sov. Phys. JETP **21**, 896 (1965).
[27]G. F. Gribakin and M. Y. Kuchiev, Phys. Rev. A **55**, 3760 (1997).
[28]H. R. Reiss, Phys. Rev. A **22**, 1786 (1980).
[29]H. R. Reiss, J. Math. Phys. **3**, 59 (1962).
[30]F. H. M. Faisal, J. Z. Kamiński, and E. Saczuk, Phys. Rev. A **72**, 023412 (2005).
[31]F. H. M. Faisal, J. Z. Kamiński, and E. Saczuk, Laser Physics **16**, 284 (2006).
[32]I. Urdaneta, A. Keller, O. Atabek, and V. Mujica, J. Phys. B **38**, 3779 (2005).
[33]C. Lemell, X.-M. Tong, F. Krausz, and J. Burgdörfer, Phys. Rev. Lett. **90**, 076403 (2003).
[34]U. Schwengelbeck, L. Plaja, E. Conejero Jarque, L. Roso, S. Varro, and Gy Farkas, J. Phys. B **35**, L181 (2002).
[35]C.-H. Zhang and U. Thumm, Phys. Rev. A **82**, 043405 (2010).
[36]C.-H. Zhang and U. Thumm, Phys. Rev. A **84**, 033401 (2011).
[37]G. D. Tsakiris, K. Eidmann, J. Meyer-ter-Vehn, and F. Krausz, New J. Phys. **8**, 19 (2006).
[38]S. I. Anisimov, V. A. Benderskii, and G. Farkas, Sov. Phys. Usp. **20**, 467 (1977).
[39]K. Mitchell, Proc. R. Soc. A **146**, 442 (1934).
[40]R. E. B. Makinson, Proc. R. Soc. A **162**, 367 (1937).
[41]D. M. Volkov, Z. Phys. **94**, 250 (1935).
[42]I. J. Berson, J. Phys. B **8**, 3078 (1975).
[43]W. Elberfeld and M. Kleber, Z. Phys. B **73**, 23 (1988).
[44]X. Antoine, A. Arnold, C. Besse, M. Ehrhardt, and A. Schädle, Commun. Comput. Phys. **4**, 729 (2008).
[45]X. Antoine, C. Besse, and P. Klein, J. Comput. Phys. **228**, 312 (2009).
[46]N. D. Lang and W. Kohn, Phys. Rev. B **7**, 3541 (1973).
[47]The distances essential for the photoelectron emission process are given by $R \simeq 1/\sqrt{\omega}$ in atomic units. This result is obtained from the uncertainty principle as it was described in Ref. 27. For a quasimonochromatic Ti:sapphire laser beam with $\hbar\omega = 1.55$ eV (800 nm), we have $R \simeq 4$ a.u.
[48]D. Bauer, D. B. Milošević, and W. Becker, Phys. Rev. A **72**, 023415 (2005).
[49]B. Bergues, Z. Ansari, D. Hanstorp, and I. Y. Kiyan, Phys. Rev. A **75**, 063415 (2007).
[50]The same coefficient appears in the theory of multiphoton stimulated bremsstrahlung of an electron in an intense laser field.[51,52] Within the first Born approximation the amplitude of a transition $p_i \to p_f$ can be written as a product $U(p_f - p_i)J_n[(p_f - p_i)eF/\omega^2]$, where $U(p)$ is the Fourier transform of the scattering potential and n denotes the number of absorbed photons (compare Eq. (2.4.4) in Ref. 51). For a flip-flop transition, i.e., when $p_f = -p_i$, we obtain $n = 0$ due to energy conservation.
[51]M. V. Fedorov, *Atomic and Free Electrons in a Strong Light Field* (World Scientific, Singapore, 1997), Sec. 2.4.
[52]F. B. Bunkin, A. E. Kazakov, and M. V. Fedorov, Usp. Fiz. Nauk **107**, 559 (1972); Sov. Phys. Usp. **15**, 416 (1973).
[53]P. Agostini, F. Fabre, G. Mainfray, G. Petite, and N. K. Rahman, Phys. Rev. Lett. **42**, 1127 (1979).
[54]T. J. McIlrath, P. H. Bucksbaum, R. R. Freeman, and M. Bashkansky, Phys. Rev. A **35**, 4611 (1987).
[55]R. R. Freeman, P. H. Bucksbaum, H. Milchberg, S. Darack, D. Schumacher, and M. E. Geusic, Phys. Rev. Lett. **59**, 1092 (1987).
[56]T. Brabec and F. Krausz, Rev. Mod. Phys. **72**, 545 (2000).
[57]L. Nordheim, Usp. Fiz. Nauk **15**, 675 (1935).
[58]N. W. Ashcroft and N. D. Mermin, *Solid State Physics* (Saunders College, Philadelphia, 1976), Chap. 13.
[59]F. W. J. Olver, *Asymptotics and Special Functions*, edited by A. K. Peters (A. K. Peters, Natick, 1997).
[60]L. D. Landau and E. M. Lifshitz, *Quantum Mechanics. Non-Relativistic Theory* (Pergamon, Oxford, 1977), Chap. 7.
[61]R. H. Fowler and L. Nordheim, Proc. R. Soc. London A **119**, 173 (1928).
[62]R. G. Forbes, J. Vac. Sci. Technol. B **26**, 788 (2008).
[63]P. Hommelhoff, C. Kealhofer, and M. A. Kasevich, Phys. Rev. Lett. **97**, 247402 (2006).
[64]A. R. Mitchel and R. Wait, *The Finite Element Method in Partial Differential Equations* (Wiley, New York, 1977).
[65]J. Crank and P. Nicolson, Proc. Cambridge Philos. Soc. **43**, 50 (1947).
[66]E. Anderson *et al.*, LAPACK *User's Guide* (Society for Industrial and Applied Mathematics, Philadelphia, 1999), Sec. 3.4.
[67]X. Antoine and C. Besse, J. Comput. Phys. **188**, 157 (2003).
[68]R. Lefebvre, Int. J. Quantum Chem. **107**, 2643 (2007).
[69]C. Tóth, G. Farkas, and K. L. Vodopyanov, Appl. Phys. B **53**, 221 (1991).
[70]A. Apolonski *et al.*, Phys. Rev. Lett. **92**, 073902 (2004).
[71]P. B. Corkum, Phys. Rev. Lett. **71**, 1994 (1993).
[72]G. G. Paulus, W. Becker, W. Nicklich, and H. Walther, J. Phys. B **27**, L703 (1994).
[73]T. F. Gallagher, Phys. Rev. Lett. **61**, 2304 (1988).
[74]P. Dombi and P. Rácz, Opt. Express **16**, 2887 (2008).
[75]B. Gottlieb, A. Lohr, W. Becker, and M. Kleber, Phys. Rev. A **54**, R1022 (1996).
[76]H. Yanagisawa, C. Hafner, P. Doña, M. Klöckner, D. Leuenberger, T. Greber, J. Osterwalder, and M. Hengsberger, Phys. Rev. B **81**, 115429 (2010).
[77]H. Yanagisawa, C. Hafner, P. Doña, M. Klöckner, D. Leuenberger, T. Greber, M. Hengsberger, and J. Osterwalder, Phys. Rev. Lett. **103**, 257603 (2009).
[78]J. G. Fujimoto, J. M. Liu, E. P. Ippen, and N. Bloembergen, Phys. Rev. Lett. **53**, 1837 (1984).
[79]J. P. Girardeau-Montaut, C. Girardeau-Montaut, S. D. Moustaizis, and C. Fotakis, Appl. Phys. Lett. **62**, 426 (1993).
[80]J. P. Girardeau-Montaut, C. Girardeau-Montaut, and S. D. Moustaizis, J. Phys. D **27**, 848 (1994).
[81]G. Ferrini, A. Viggiani, D. Sertore, P. Michelato, and F. Parmigiani, Phys. Rev. B **60**, 8383 (1999).
[82]J. P. Girardeau-Montaut and C. Girardeau-Montaut, Phys. Rev. B **51**, 13560 (1995).